COVER PAGE

Bibliographical reference

An Efficient Finite Element Model for Viscothermal Acoustics, W. R. Kampinga, Y. H. Wijnant and A. De Boer, Acta Acustica **vol. 97** (Number 4), 2011, pp. 618-631

DOI
https://doi.org/10.3813/AAA.918442

Acta Acustica united with Acustica
Vol. 97 (2011) 618 – 631

DOI 10.3813/AAA.918442

An Efficient Finite Element Model for Viscothermal Acoustics

W. R. Kampinga, Y. H. Wijnant, A. de Boer
University of Twente, Enschede, Netherlands. W.R.Kampinga@CTW.UTwente.nl

Summary
Standard isentropic acoustic models do not include the dissipative effects of viscous friction and heat conduction. These viscothermal effects can be important, for example in models of small acoustic transducers. Viscothermal acoustics can be modeled in arbitrary geometries with models that contain four or five coupled fields. Therefore, these fully coupled models are computationally costly. On the other hand, efficient approximate viscothermal acoustic models exist, but these are only applicable to certain simplified geometries. A new approximate model is presented which fills the gap between these two extremes. This new model can be used for arbitrary geometries and has a computational efficiency which is higher than the full model and lower than the models with geometrical constraints. The new model is derived and demonstrated on several problems, including acoustic-structure interaction problems.

PACS no. 43.20.-f, 43.20.Bi, 43.20.Tb

1. Introduction

Viscothermal acoustics, unlike normal (isentropic) acoustics, includes the dissipative boundary layer effects of heat conduction and viscous friction. These effects can be significant, especially in geometries with small characteristic length scales. Several finite element formulations of viscothermal acoustics are presented in the literature, for example [1, 2, 3]. These *full models* have two important properties in common:

1. Arbitrary geometries can be modeled.
2. The models are computationally costly.

The high computational costs are evident considering that five (or four) coupled fields are calculated on a FEM mesh that should be fine in the boundary layers.

Besides the referred full models of viscothermal acoustics, several *approximating models* are presented in the literature. These models are computationally efficient (the computational costs are comparable to isentropic acoustics), but can not be used for arbitrary geometries. Two examples of such models are the low reduced frequency (LRF) model [4, 5, 6] and the boundary layer model of Bossart [7]. The LRF model is only applicable to waveguides below the cut-off frequency with uniform or slowly varying cross sections, and Bossart's model is only applicable to geometries of which all characteristic lengths are much larger than the boundary layer thickness.

This paper presents a new approximating viscothermal acoustic model that can be applied to arbitrary geometries, but is much more efficient than the full models. This new model uses similar approximations as the LRF model and Bossart's model. The new model of this paper is referred to as the *Sequential Linearized Navier-Stokes* (SLNS) model, because (like in the LRF model and Bossart's model) the viscous and thermal fields are calculated first and the acoustic pressure field thereafter.

Received 28 June 2010,
accepted 4 February 2011.

2. Theory

The Sequential Linearized Navier-Stokes (SLNS) model is derived in this section. The order of magnitude analysis on which the derivation is based is presented in the appendix. The derivation of the SLNS model starts with the full linear Navier-Stokes equations.

2.1. Full Linearized Navier-Stokes equations

The standard formulation for viscothermal acoustics is a set of Navier-Stokes equations that is linearized under assumption of small acoustic perturbations. These equations are often given in time harmonic form (based on $e^{i\omega t}$ in this paper, not $e^{-i\omega t}$) with the complex perturbation fields (phasors) of the velocity vector $\boldsymbol{v}$, temperature T and pressure p as the variables. This set of viscothermal acoustic equations for a Newton-Fourier ideal gas reads, see for example [8, 9, 10, 11, 1],

$$\mathrm{i}\omega\rho_0\boldsymbol{v} - \nabla\cdot\boldsymbol{\tau} + \nabla p = \boldsymbol{f}, \tag{1a}$$

$$\mathrm{i}\omega\rho_0 C_p T + \nabla\cdot\boldsymbol{q} - \mathrm{i}\omega p = Q, \tag{1b}$$

$$\nabla\cdot\boldsymbol{v} - \mathrm{i}\omega\frac{T}{T_0} + \mathrm{i}\omega\frac{p}{p_0} = 0, \tag{1c}$$

with i, ω, ρ_0, T_0, p_0 and C_p the imaginary unit, angular frequency, quiescent density, quiescent temperature, qui-

escent pressure and specific heat at constant pressure respectively. Furthermore, $\boldsymbol{f}$ and Q are the complex amplitudes of the harmonic body (volume) forces and heat sources, which often equal zero. The viscous damping results from the divergence of the viscous tensor $\boldsymbol{\tau}$ and the thermal damping from the divergence of the heat flux $\boldsymbol{q}$. These terms are defined as function of the velocity and temperature variables as

$$\nabla \cdot \boldsymbol{\tau} = (\lambda + \mu)\nabla(\nabla \cdot \boldsymbol{v}) + \mu \Delta \boldsymbol{v}, \tag{2}$$

$$\nabla \cdot \boldsymbol{q} = -\kappa \Delta T, \tag{3}$$

with λ, μ and κ the second viscosity, dynamic viscosity and heat conduction coefficient. The set of equations (1) can be reduced to the isentropic acoustic Helmholtz equation if both $\boldsymbol{\tau} = \mathbf{0}$ and $\boldsymbol{q} = 0$ (and $\boldsymbol{f} = 0$, $Q = 0$).

The given three equations are the momentum equation (1a), the entropy or enthalpy equation (1b), and the continuity equation (1c). The continuity is often formulated in terms of the density perturbation, but here the pressure and temperature are used instead. The linearized ideal gas law

$$\frac{\rho}{\rho_0} = \frac{p}{p_0} - \frac{T}{T_0} \tag{4}$$

has been used to yield this result.

2.2. Boundary conditions and properties of solutions

A distinction in a boundary layer region and a bulk region can typically be made in viscothermal acoustic solutions; see Figure 1. The bulk vanishes if the geometry is made very small, but the present discussion considers the case that does have a bulk for convenience. Standard isentropic acoustic models accurately describe the wave propagation in the bulk. However, the viscous and thermal effects are important in the boundary layer region. These effects cause high perpendicular gradients (in the direction denoted as $x_\perp$ in the figure) in the temperature and shear velocity fields, dependent on the prescribed boundary conditions. Typically, an isothermal (zero temperature perturbation) boundary condition causes a thermal boundary layer. Likewise, a no-slip (zero shear velocity perturbation) boundary condition causes a viscous boundary layer. The viscous and thermal effects damp the propagation of the acoustic wave. Unlike the temperature and shear velocity fields, the pressure and normal velocity fields remain relatively smooth in the boundary layer.

Three types of boundary conditions can be prescribed in viscothermal acoustics

1. *Thermal boundary conditions:* temperature, heat flux or thermal impedance (temperature dependent heat flux).
2. *Viscous boundary conditions:* shear velocity, shear force or viscous impedance (shear velocity dependent force).
3. *Acoustic boundary conditions:* normal velocity, pressure or acoustic impedance (normal velocity dependent pressure).

In 3-D geometries, there are two shear velocity components and therefore two viscous boundary conditions: one for each direction.

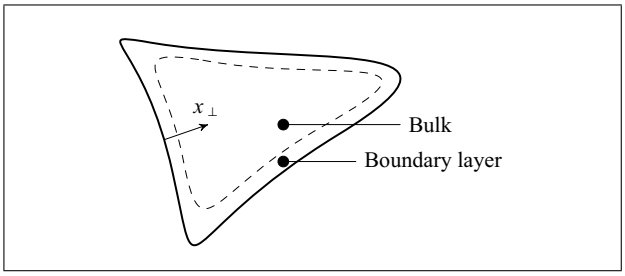

Figure 1. Viscothermal acoustic solution with bulk region and boundary layer region.

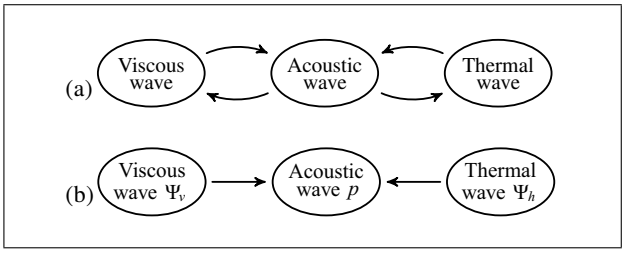

Figure 2. Viscothermal acoustics is a three wave theory. The full model of equation (1) is schematically shown in (a) in which the three waves are coupled. This paper presents a sequential model that is shown schematically in (b). The LRF model and Bossart's model use a similar decoupling.

2.3. Sequential Linearized Navier-Stokes model

Like the boundary conditions just described, the solution itself can be divided into three parts: the acoustic wave, the viscous wave and the thermal wave. It may be confusing to label all three parts as waves, because only acoustics is usually thought of as wave propagation. The viscous and thermal effects are actually diffusion processes [3, 10]. Nevertheless, in time harmonic form, the diffusion resembles a highly damped wave. Therefore, the three wave paradigm is convenient and often used; see for example [11, 12].

This paper presents a model that approximates the fully coupled three waves as three waves that are only coupled in one direction; see Figure 2. The acoustic wave is represented by the pressure field p and the viscous and thermal waves by the scalar fields Ψ_v and Ψ_h respectively. The definition of these viscous and thermal waves becomes clear later.

2.3.1. Reduced set of equations

The full set of equations (1) is reduced by approximations that are based on the order of magnitude analysis presented in the appendix. The approximations for the SLNS model resemble those in the LRF model [6, 4, 5]. The important difference is that the LRF model's derivation uses a *global* split in propagation and cross section directions, while the the SLNS model's derivation only uses a *local* split near boundaries in normal and tangential directions.

The term that accounts for the viscous effects, equation (2), is approximated as

$$\nabla \cdot \boldsymbol{\tau} = \mu \Delta \boldsymbol{v}. \tag{5}$$

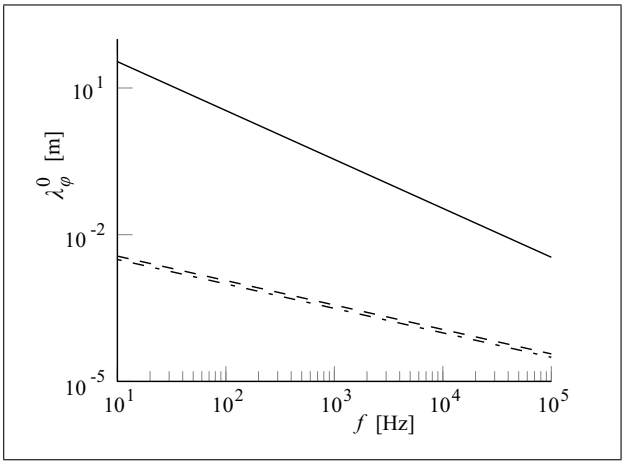

Figure 3. The acoustic wave length is larger than the viscous and thermal boundary layer thicknesses in air; (——) isentropic acoustic wavelength λ_0; (– - –) viscous boundary layer thickness λ'_v; (– – –) thermal boundary layer thickness λ'_h.

This approximation neglects the terms that are expected to be small: the divergence of the velocity is much smaller than the gradient of the velocity; see the appendix.

The above approximation and the assumptions $\boldsymbol{f} = 0$ and $Q = 0$ allow to rewrite the full set of equations (1) as

$$\boldsymbol{v} + k_v^{-2}\Delta\boldsymbol{v} = \frac{-\nabla p}{ik_0 Z_0}, \tag{6a}$$

$$T + k_h^{-2}\Delta T = \frac{p}{\rho_0 C_p}, \tag{6b}$$

$$\nabla\cdot\boldsymbol{v} - i\omega\frac{T}{T_0} + i\omega\frac{p}{p_0} = 0. \tag{6c}$$

with $\gamma \equiv C_p/C_v$ the ratio of specific heats. The set of equations (6) contains the isentropic acoustic wave number k_0 and characteristic impedance Z_0 that are defined as

$$k_0 \equiv \omega/c_0, \qquad Z_0 \equiv \rho_0 c_0. \tag{7}$$

Furthermore, the viscous wave number k_v and thermal wave number k_h in the set of equations are defined as

$$k_v^2 \equiv -\mathrm{i}\omega\rho_0/\mu, \quad k_h^2 \equiv -\mathrm{i}\omega\rho_0 C_p/\kappa. \tag{8}$$

These squared wave numbers are purely imaginary because they represent diffusion processes.

The relation of the acoustic wave number to the wave length $\lambda_0 = 2\pi/k_0$ is similar to the relation of the viscous and thermal wave numbers to the viscous and thermal boundary layer thicknesses: $\lambda'_v = 2\pi/\left|k_v\right|$ and $\lambda'_h = 2\pi/\left|k_h\right|$. Figure 3 shows that the viscous and thermal boundary layer thicknesses are much smaller than the acoustic wavelength in air for the plotted frequency range. The difference in the acoustic wave number versus the viscous and thermal wave numbers are important in the order of magnitude analysis on which the SLNS model is based; see the appendix.

2.3.2. Approximate solutions

The momentum equation (6a) and the entropy equation (6b) can be regarded as non-homogeneous Helmholtz equations of the velocity and temperature. These equations describe the viscothermal boundary layer effects which are highly damped diffusion waves. As shown in Figure 3, the boundary layer thicknesses are much smaller than the acoustic wave length. Therefore, the pressure and pressure gradient terms in the right hand sides are typically very smooth in comparison. This makes the following solutions of the shear velocity $\boldsymbol{v}_\parallel$ and temperature accurate:

$$\boldsymbol{v}_\parallel = \Psi_v\frac{-\nabla_\parallel p}{\mathrm{i}k_0 Z_0}, \tag{9}$$

$$T = \Psi_h\frac{p}{\rho_0 C_p}, \tag{10}$$

where Ψ_v and Ψ_h are *scalar* viscous and thermal fields that should satisfy the partial differential equations

$$\Psi_v + k_v^{-2}\Delta\Psi_v = 1, \tag{11}$$

$$\Psi_h + k_h^{-2}\Delta\Psi_h = 1. \tag{12}$$

The accuracy of the solutions (9) and (10) are verified in the appendix. The approximation is based on the different magnitudes of the acoustic wave number versus the viscous and thermal wave numbers.

The solutions of the temperature and shear velocity are valid for homogeneous viscous and thermal boundary conditions. The viscous boundary condition is prescribed to the viscous field and follows from the shear velocity solution (9),

$$\Psi_v = 0 \qquad \text{(no-slip)}, \tag{13a}$$

$$\nabla_n\Psi_v = 0 \qquad \text{(no-shear-force)}, \tag{13b}$$

with $\nabla_n = \boldsymbol{n}\cdot\nabla$. The no shear force boundary condition is an approximation that is discussed in the appendix. Similarly, the thermal boundary condition is prescribed to the thermal field and follows from the temperature solution (10),

$$\Psi_h = 0 \qquad \text{(isothermal)}, \tag{14a}$$

$$\nabla_n\Psi_h = 0 \qquad \text{(adiabatic)}, \tag{14b}$$

where the adiabatic boundary condition is again an approximation that is discussed in the appendix.

Notice that the calculation of the viscous and thermal fields, Ψ_v and Ψ_h, does not require knowledge of the acoustics field (pressure p). Therefore, these fields are decoupled as was illustrated by Figure 2b.

The viscous and thermal fields are approximately unity in the bulk of the domain. Near no-slip and isothermal walls, the fields reduce to zero. For example, the cross section of the viscous and thermal fields along $x_\perp$ in Figure 1 is plotted in Figure 4. The shape of this field changes if the boundary has a high curvature, or if the opposite boundary is nearby. The indicated distances in the figure are the already introduced boundary layer thickness $\lambda'_\phi = 2\pi/\left|k_\phi\right|$, another frequently used boundary layer thickness measure $\delta'_\phi = -1/\Im(k_\phi)$ and the wave length $\lambda_\phi = 2\pi/\Re(k_\phi)$; where $\Im$ and $\Re$ denote the imaginary and real part.

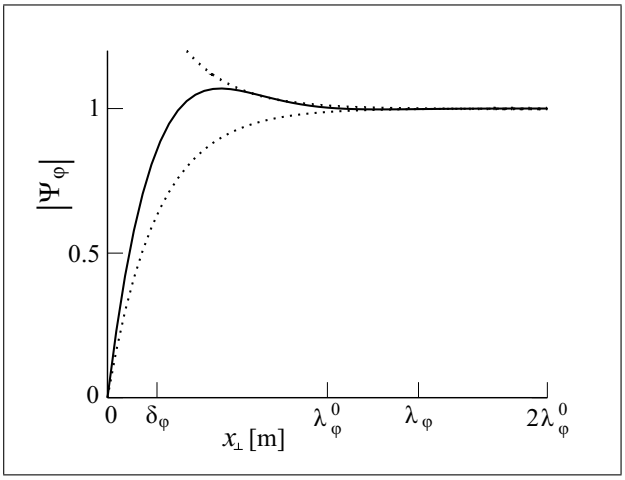

Figure 4. Typical shape of the magnitude of the viscous and thermal fields near a no-slip isothermal wall. The boundary layer shape (——) and its envelope function (· · ·).

The approximate solution of the temperature (10) allows to simplify the expression of the density (4) to

$$\rho = \frac{\Psi'_h p}{c_0^2}. \tag{15}$$

This expression is derived by using several ideal gas identities: $C_p = R_0 + C_v$ with R_0 the specific gas constant and C_v the specific heat at constant volume, the ideal gas law applied to the quiescent field values $p_0 = \rho_0 R_0 T_0$, and the *isentropic* speed of sound c_0 in an ideal gas $c_0^2 = \gamma p_0/\rho_0$. The symbol Ψ'_h represents the modified thermal field defined as

$$\Psi'_h \equiv \gamma - (\gamma - 1)\Psi_h. \tag{16}$$

In a similar derivation as for the approximate density, the approximate continuity equation can be obtained, resulting in

$$-\mathrm{i}k_0 Z_0 \nabla \cdot \boldsymbol{v} + k_0^2 \Psi'_h p = 0. \tag{17}$$

This continuity equation in combination with the acoustic boundary conditions will be used to calculate the pressure.

2.3.3. Weak formulations for FEM

Three sequential finite element calculations are needed: the viscous field, the thermal field and the pressure field. The weak forms of the viscous and thermal fields are presented separate from the weak form of the pressure field. The notation in this section uses the Hermitian inner products

$$\left\langle \Psi_w, \Psi \right\rangle \equiv \int_\Omega \overline{\Psi_w} \cdot \Psi \, \mathrm{d}\Omega, \tag{18}$$

$$\left\langle \Psi_w, \Psi \right\rangle_{\partial\Omega} \equiv \int_{\partial\Omega} \overline{\Psi_w} \cdot \Psi \, \mathrm{d}\partial\Omega, \tag{19}$$

with Ω the domain and $\partial\Omega$ its boundary. In general, the inner product's subscript denotes the region of integration, but this is omitted if the region equals the domain Ω. The entries in this inner products (Ψ_w and Ψ) may be two scalars or two vectors. The line over Ψ_w denotes a complex conjugation. It may be omitted in the weak forms, because Ψ_w is a real valued weighing function.

Viscous and thermal fields

The calculation of the viscous fields and the thermal fields are similar. The weak forms of equations (11) and (12) are given as

$$\left\langle \Psi_w, \Psi_\phi \right\rangle - k_\phi^{-2} \left\langle \nabla\Psi_w, \nabla\Psi_\phi \right\rangle = \left\langle \Psi_w, 1 \right\rangle - k_\phi^{-2} \left\langle \Psi_w, h_\phi \right\rangle_{\partial\Omega} \tag{20}$$

in which ϕ is a dummy variable that can be replaced by v or h for the viscous or the thermal field and h_ϕ is the natural boundary condition term that is given below. Furthermore, Ψ_w denotes the weighing functions.

The boundary conditions (BCs) for the viscous and thermal fields should be homogeneous. Equations (13a) and (14a) are essential boundary conditions of the weak form, and equations (13b) and (14b) are natural boundary conditions:

$$\Psi_\phi = 0 \qquad \text{(no slip / isothermal BC)}, \tag{21a}$$

$$h_\phi = 0 \qquad \text{(no shear force / adiabatic BC)}. \tag{21b}$$

The no shear force and adiabatic BCs are approximations, as mentioned above. One viscous BC and one thermal BC should be prescribed on each boundary location.

Acoustic pressure field

The pressure field is calculated with the continuity equation (17). The weak form of this equation is

$$\mathrm{i}k_0 Z_0 \left\langle \nabla p_w, \boldsymbol{v} \right\rangle + k_0^2 \Psi'_h \left\langle p_w, p \right\rangle = \mathrm{i}k_0 Z_0 \left\langle p_w, \boldsymbol{v} \cdot \boldsymbol{n} \right\rangle_{\partial\Omega}. \tag{22}$$

This weak form is simplified by substitution of the approximate expression of the shear velocity (9) in the left hand side of this weak form. The perpendicular component of the velocity is chosen similar, such that total velocity vector is

$$\boldsymbol{v} = \Psi_v \frac{-\nabla p}{\mathrm{i}k_0 Z_0}. \tag{23}$$

The resulting weak form after the substitution is

$$-\Psi_v \left\langle \nabla p_w, \nabla p \right\rangle + k_0^2 \Psi'_h \left\langle p_w, p \right\rangle = \mathrm{i}k_0 Z_0 \left\langle p_w, \boldsymbol{v} \cdot \boldsymbol{n} \right\rangle_{\partial\Omega}. \tag{24}$$

This weak form closely resembles the weak form of the isentropic acoustic Helmholtz equation. It is identical if $\Psi_v = \Psi'_h = 1$. This condition is true in the bulk of the domain.

The above weak form should satisfy the acoustic boundary conditions, which may include *fluid structure interaction*. The pressure is an essential boundary condition and the normal velocity is a natural boundary condition prescribed with the boundary integral at the right-hand side of equation 24. An impedance can be prescribed as a pressure dependent velocity natural boundary condition. The above weak form has one issue with respect to the normal velocity component, which is discussed next.

2.3.4. Normal velocity

There is one potential problem with the weak form of the pressure field (24). Its derivation used equation (9) for the perpendicular velocity component, while it is only valid for the shear velocity components. This leads to an inconsistent set of boundary conditions in one case: both $\Psi_v = 0$ (no-slip) and $v_n \neq 0$ (non-homogeneous normal velocity). The normal velocity in equation (23) becomes zero despite the non-zero boundary condition in this case. The prescription of these boundary conditions is possible, because the normal velocity is prescribed with a natural BC, independent of the viscous boundary condition, but this inconsistency does leads to errors. Fortunately, these errors are small as will be shown in section 3.2.

The normal velocity inconsistency might be removed from the model by using the normal velocity expression from the isentropic acoustic Euler equation:

$$v_\perp = \frac{-\nabla_\perp p}{\mathrm{i}k_0 Z_0} \tag{25}$$

This isentropic acoustic expression is an accurate approximation of the normal velocity in the viscothermal acoustics case. The effect of the viscothermal boundary layers on the normal velocity is very small; see [7, 8, 9, 13]. The weak form based on this normal velocity can be written as

$$\begin{aligned} -\Psi_v \left\langle \nabla p_w, \nabla p \right\rangle - (1-\Psi_v)\left\langle \nabla_\perp p_w, \nabla_\perp p \right\rangle \\ + k_0^2 \Psi_h' \left\langle p_w, p \right\rangle = \mathrm{i}k_0 Z_0 \left\langle p_w, \boldsymbol{v}\cdot\boldsymbol{n} \right\rangle_{\partial\Omega}. \end{aligned} \tag{26}$$

The drawback of this weak form is that it needs a robust and generally applicable implementation of the perpendicular gradient $\nabla_\perp$ in the boundary layer. Unfortunately, the authors have not found one, which makes the above weak form unusable. Therefore the weak form (24) is used instead.

The problems with the normal velocity inconsistency in the weak form (24) is the following: the inconsistency leads to a large pressure gradient near the inconsistent boundary, trying, unsuccessfully, to prevent equation (23) from approaching zero. This large pressure gradient also affects the pressure itself, but fortunately not as much, because the erroneous region is very small. Section 3.2 will show good results without additional measures. Even better results can be obtained by following two basic rules

1. Do *not* use a very fine boundary layer mesh for the pressure calculation.
2. Neglect the viscous effects at the concerned boundary by using a no-shear-force BC, if the wave is likely to propagate perpendicular to the moving boundary.

The largest erroneous pressure gradient is expected *at* the inconsistent boundary where $\Psi_v = 0$. The smaller the element at the boundary, the larger the pressure gradient will become. The error is smoothed if the element size increases, resulting in the first rule. The second rule is to circumvent the inconsistency. It is only accurate if the viscous effects are insignificant, which is for waves that propagate perpendicular to the concerned boundary, see again [7, 8, 9, 13]. The effectiveness of these rules is demonstrated in section 3.2.3.

2.3.5. Algorithm of the SLNS model

Summarizing, the new SLNS model presented in this paper involves three sequential calculations

1. Calculate the thermal field with FEM using the weak form (20) and the boundary conditions (21); substituting h for ϕ.
2. Calculate the viscous field with FEM using the weak form (20) and the boundary conditions (21); substituting v for ϕ.
3. Calculate the pressure with FEM using the weak form (24) and essential pressure boundary conditions and/or natural normal velocity or acoustic impedance boundary conditions.

Step 1 and 2 may be combined in a single FEM calculation. The third step depends on the first two steps and should be performed last. Quadratic Lagrangian shape functions are used for all fields (Ψ_h, Ψ_v, p).

This viscothermal acoustic model involves the calculation of three *uncoupled* scalar fields. By contrast, the full viscothermal acoustic model based on the set of equations (1) involves a calculation of five (or four) *coupled* fields. Therefore, the new SLNS model is much more efficient.

2.4. Comparing the SLNS model to other models

Quite a large number of viscothermal acoustic models already exist. The new SLNS model is compared to models that may be interesting alternatives for some specific cases. The difference between SLNS model and the full Navier-Stokes model is explained in the theory above. This section compares the SLNS model to the semi-analytical Kirchhoff solution methods for the full viscothermal acoustic Navier-Stokes model, Bossart's boundary layer model, the Low Reduced Frequency model, and to plain isentropic acoustics.

2.4.1. Comparison with classical Kirchhoff models

Kirchoff's classical solution methods for the full viscothermal acoustic equations contain a few steps, see [4, 10, 11, 14] for example:

1. Split the velocity vector in a rotation free and a divergence free part (or apply a Helmholtz decomposition to it). Substitute this velocity expression into the equations. The momentum equation for the divergence free velocity component decouples as a Helmholtz equation (or equivalent under the constraint of zero divergence) with a wave number that is denoted as k_v.
2. The remaining equations are manipulated to fourth order differential equations of the form $(\Delta + k_h^2)(\Delta + k_a^2)T = 0$, and identical for the pressure and the rotation free part of the velocity (or the velocity potential).
3. The PDE's are now decoupled and analytic solutions can be formulated for *simple geometries* up to a (possibly infinite) series of unknowns that depend on the boundary conditions. Unfortunately, the boundary conditions are not decoupled. Manipulation of the boundary conditions and the analytic solutions results in a *dispersion equation*. The unknowns of the analytic solution are the

roots of the dispersion equation, which can be found by using numerical methods.

The Kirchhoff method is an approximation of the full equations in the sense that solution is an truncated series, whereas the SLNS model is an approximation by elimination of smaller terms in the PDEs. In theory, the Kirchhoff methods lead to solutions that can be made more accurate by adding more terms. On the other hand, the Kirchhoff method is only used on simple geometries in the literature, whereas the SLNS model is for arbitrary geometries. Furthermore, the SLNS model is easier to use is FEM software that accepts user defined weak forms is available.

The wave numbers k_v and k_h used in the Kirchhoff methods are similar but not identical to the wave numbers in SLNS model, which are given the same symbols in this paper. In fact the wave numbers k_v and k_h in the SLNS model are an low order approximation (according to the definition from the appendix) of the wave numbers k_v and k_h of the Kirchhoff models. Furthermore, k_0 is a low order approximation of k_a by the same definition.

2.4.2. Comparison with Bossart's model

Cremer's impedance boundary condition [13, 8, 9] accounts for viscothermal losses in isentropic acoustics. The model of Bossart [7] uses this boundary condition in a numerical solution method. The paper [7] demonstrates the method with boundary elements but the formulation easily translates to finite elements. Only the scalar isentropic acoustic Helmholz equation of the pressure must be solved (twice) and the viscothermal dissipation is taken into account by (complex valued) impedance boundary conditions. Unfortunately, this model is inaccurate if narrow parts of the geometry are comparable in thickness to the boundary layer thickness, see section 3.1.2 for an example.

Unlike Bossart's model, the SLNS is applicable to arbitrary geometries. Nevertheless, when Bossart's model is applicable, it is recommended above the SLNS model because of the lower computational costs.

2.4.3. Comparison with the LRF model

The LRF model is an efficient model for waveguides below the cutoff frequency (narrower than the acoustic wavelength). Like in isentropic acoustic waveguide models, the pressure field is assumed to be uniform across the waveguide's section. If it is not uniform, like in waveguides with rapidly changing cross sections, the LRF solution becomes inaccurate, see section 3.1.2 for an example. By contrast, the SLNS model is for arbitrary geometries.

The SLNS model and the LRF model have more in common than the above suggests. The SLNS model could even be regarded as a more general version of the LRF model. In fact, the LRF model is easily derived from the SLNS model in the following steps:

1. Split the coordinates, spatial derivatives and velocity vector in the propagation direction of the wave guide and the cross section direction that is perpendicular to it. Apply this split to the gradients and velocities in the approximate solutions from section 2.3.2.
2. Assume a pressure that is uniform over the cross section, and neglect the effects of the gradients in the propagation direction on the viscous and thermal fields.
3. Use the average of the viscous and thermal fields over the cross section instead of the distributed fields themselves.

The average viscothermal fields are typically determined analytically. Therefore, the LRF model is essentially a one-dimensional model (for tubes) or two-dimensional model (for layers) in which only the scalar pressure field has to be solved. This makes the LRF model very efficient. It is recommended above the SLNS model for all problems with uniform or slowly varying waveguides below the cut-off frequency. The SLNS model is interesting for cases than cannot be accurately described by the LRF model.

Interestingly, the LRF model does not have the normal velocity inconsistency that the SLNS model has, because normal velocities at boundaries are not applied as boundary conditions, but as internal volume sources. This is an interesting method that may work in the SLNS model as well. The normal velocity could be included as a volume source in the elements near the boundary. The main drawback of this method is that it requires the programming of a routine that is non-standard in FEM to make it work for arbitrary geometries. Therefore, this method is not evaluated in this paper.

2.4.4. Comparison with isentropic acoustics

The weak form of the (decoupled) pressure field (24) of the SLNS model can be compared to the weak form of the isentropic acoustic pressure field; see [15]. This comparison shows that the viscous effects are taken into account as the pressure gradient dependent dipole source $(1-\Psi_v)\nabla p$. Similarly, the thermal effects are taken into account as the pressure dependent monopole source $k_0^2(\Psi_h' - 1)p/\rho_0$. In the bulk of the domain, The viscothermal fields equal unity and the monopole and dipole sources vanish, but in the boundary layer these sources result in the viscothermal damping.

3. Results

Because of the potential issues with non-zero normal velocity boundary conditions, discussed in section 2.3.4, the results are divided into two parts: one for fixed walls and one for moving walls. All models use the air properties listed in Table I. The FEM software COMSOL [15] is used for all FEM calculations.

3.1. Fixed walls

The SLNS model is compared to accurate analytic solutions for waveguides and to measurements with impedance tube samples that have a more complicated geometry. Results of other viscothermal acoustic models are shown for additional comparison.

Table I. The properties of air used in all models.

Symbol	Value	Unit
T_0	294.3	K
p_0	$1.015 \cdot 10^5$	Pa
c_0	341.2	m/s
ρ_0	1.225	kg/m^3
κ	$25.18 \cdot 10^{-3}$	W/(m K)
μ	$18.29 \cdot 10^{-6}$	Pa s
λ	$-1.22 \cdot 10^{-6}$	Pa s
γ	1.406	1
R_0	281.4	J/(kg K)
C_p	975.3	J/(kg K)
C_v	693.8	J/(kg K)

Table II. Boundary conditions for the SLNS model.

Type	Symbol	Boundary conditions		
		Acoustic	Viscous	Thermal
Wall	$\partial\Omega_W$	$v_n = 0$	$\Psi_v = 0$	$\Psi_h = 0$
Symmetry	$\partial\Omega_S$	$v_n = 0$	$h_v = 0$	$h_h = 0$
Pressure	$\partial\Omega_P$	$p = 1$	$h_v = 0$	$h_h = 0$
Open	$\partial\Omega_{P_0}$	$p = 0$	$h_v = 0$	$h_h = 0$

3.1.1. Waveguides

Uniform waveguides are accurately described by the low reduced frequency model, provided that they are narrow with respect to the wave length and that the inlet effects are negligible. The slit problem (2-D) in Figure 5 has the following analytic low reduced frequency model solutions for the pressure and velocity

$$\hat{p} = \frac{\cos(k_\ell x)}{\cos(k_\ell L)}, \quad \hat{v}_x = \frac{\hat{\Psi}_v/\hat{\Upsilon}_v}{iZ_\ell}\frac{\sin(k_\ell x)}{\cos(k_\ell L)}, \tag{27}$$

with the velocity and temperature profiles $\hat{\Psi}_v$ and $\hat{\Psi}_h$ and their mean values over the cross-section $\hat{\Upsilon}_v$ and $\hat{\Upsilon}_h$

$$\hat{\Psi}_\phi = 1 - \frac{\cos\left(k_\phi z\right)}{\cos\left(k_\phi \ell/2\right)}, \tag{28}$$
$$\hat{\Upsilon}_\phi = 1 - \frac{\tan\left(k_\phi \ell/2\right)}{k_\phi \ell/2},$$

in which ϕ is a dummy index that can be replaced by v or h. Furthermore, the modified mean thermal field is defined as $\hat{\Upsilon}'_h = \gamma - (\gamma - 1)\hat{\Upsilon}_h$, the characteristic wave number and impedance of the waveguide as

$$k_\ell^2 \equiv k_0^2 \frac{\hat{\Upsilon}'_h}{\hat{\Upsilon}_v}, \qquad Z_\ell^2 \equiv \frac{Z_0^2}{\hat{\Upsilon}'_h \hat{\Upsilon}_v}. \tag{29}$$

Notice the similarities between the structure of the LRF model and the SLNS model.

Only half of the geometry has to be modeled in FEM, because the problem is symmetric. The boundary conditions that are shown in Figure 5 are explained in Table II.

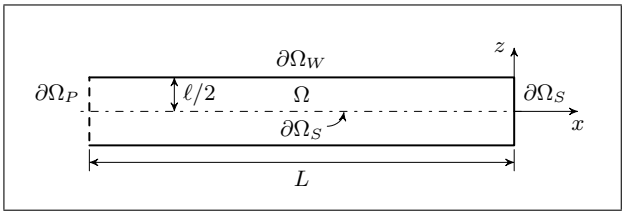

Figure 5. Slit problem: the slit ($L = 0.1$ m) has a pressure source at the left-hand side and is closed at the right-hand side. Only half the geometry is modeled in the SLNS model because of symmetry, as indicated by Ω. The boundary conditions are explained in Table II.

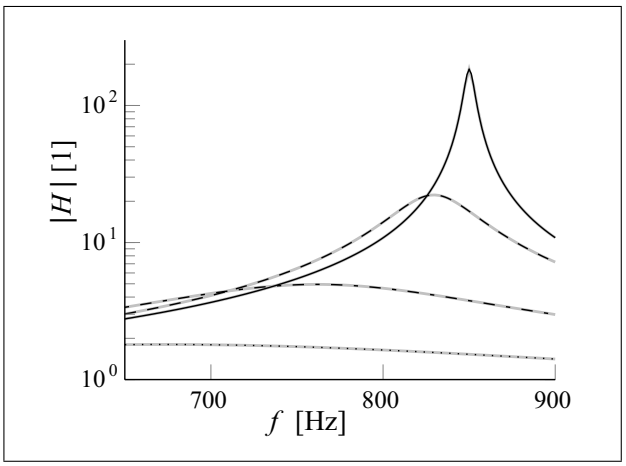

Figure 6. Pressure transfer function of the slit problem. The LRF model is used as the reference with slit thickness ℓ 16 mm (——), 2 mm (– – –), 0.5 mm (– - –), 0.25 mm (· · ·). The curves of the SLNS model (——) match the LRF curves well.

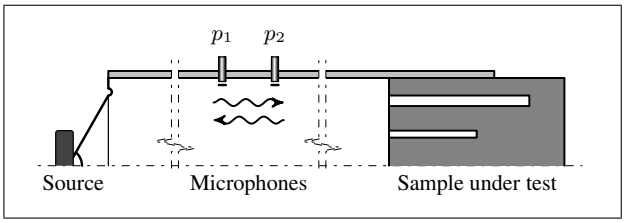

Figure 7. Axi-symmetric schematic drawing of an impedance tube. The use impedance tube has a diameter of 5 cm.

The SLNS model is compared to the analytic LRF solution for several slit thicknesses ℓ in Figure 6. The plotted quantity is the absolute value of the transfer function $H = p|_{x=0}/p|_{x=-L}$. The results of the two models match very well.

3.1.2. Impedance tube samples

Application of the SLNS model to more complicated geometries is demonstrated by two impedance tube samples. An impedance tube is an acoustic measurement device that can be used to determine the absorption coefficient of a sample. Figure 7 shows a schematic drawing of it. The tube is narrow compared to the acoustic wavelength such that wave propagation can be regarded as one-dimensional in the measurement section in the middle of the tube. The

acoustic behavior may be more complicated at the source and at the sample. Two microphones are placed in the measurement section. The measured signals can be used to calculate the absorption coefficient of the sample, using the transfer function $H_{it} = p_2/p_1$. This transfer is estimated with standard spectral methods in the real setup. In the FEM models, it is calculated at each frequency by simple division of the (complex valued) pressures at the two locations. The absorption coefficient α given as function of H_{it} is

$$\alpha = 1 - \left| \frac{e^{-ik_0 d} - H_{it}}{H_{it} - e^{ik_0 d}} \right|^2, \tag{30}$$

with $d = 45$ mm, the distance between the two microphones. The absorption coefficient has a value between 0 (no absorption) and 1 (full absorption). Two acoustically hard resonators are measured and modeled. If isentropic acoustic models were to be used, a zero valued absorption coefficient would be found for all frequencies (except perhaps exactly at a resonance frequency). In other words, all non-zero values that are calculated are directly caused by viscothermal dissipation.

The first resonator is axi-symmetric and shown in Figure 8. This sample is developed by Jansen [16]. The wall of the impedance tube is modeled without viscothermal effects (slip, adiabatic BCs) to reduce the required degrees of freedom: the mesh at this boundary can be coarser if there are no boundary layers. The sample has a rapidly varying cross section and several narrow passages in which viscous effects are important.

The absorption coefficient curves of a measurement and several viscothermal acoustic models are shown in Figure 9. The two absorption coefficient peaks are at the first two acoustic resonance frequencies of the sample. The full model and the new SLNS model both accurately correspond to the measured curve. Two curves from other models are not as accurate, because the modeled sample does not meet the requirements of these models. The low reduced frequency model is inaccurate because it is only valid for slowly varying waveguides, while the sample's cross section varies rapidly. The model of Bossart is not accurate because it is only valid for relatively large geometries, while the sample contains narrow passages.

Thus only the full model and the SLNS model are accurate for Jansen's sample. These models both use the same FEM mesh. The computational costs are compared in Table III. The SLNS model is more than 6 times faster in this case. The LRF model and Bossart's model are faster because the number of degrees of freedom is smaller: a coarser mesh is used for Bossart's model (since only the smooth pressure field has to be described), and a 1-D mesh is used for the LRF model (only the pressure field that is assumed uniform over the cross section is described). Unfortunately, these two models are inaccurate for this sample. This makes the new SLNS model a useful addition to the existing viscothermal acoustic models.

A photo of the second sample is shown in Figure 10. This sample is developed by Hannink [17] to demonstrate

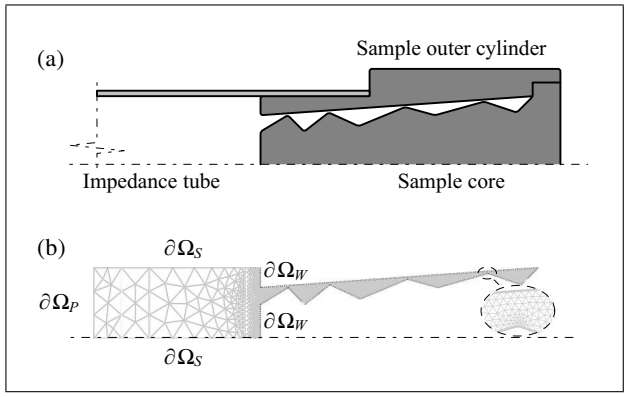

Figure 8. Jansen's sample, axi-symmetric cross section. (a) Construction, (b) FEM model.

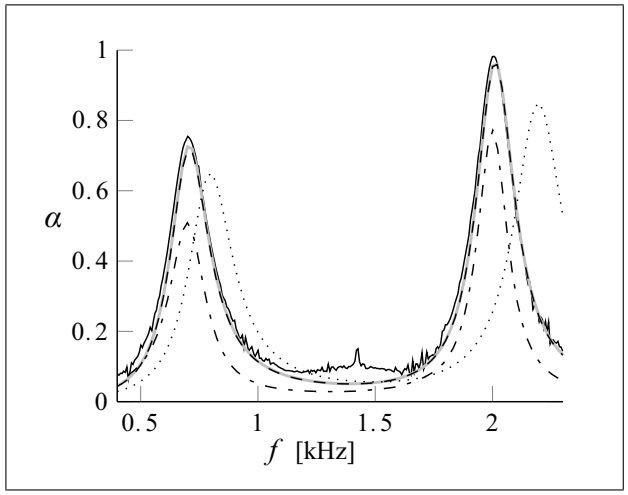

Figure 9. Absorption coefficient of Jansen's sample: (——) measurement; (——) full model; (– – –) SLNS model; (– - –) Bossart's model; (· · ·) LRF model.

Table III. Calculation time per frequency (t_c) and number of DOFs in the different models for Jansen's sample. The full and SLNS model use the same FEM mesh.

Model	t_c [s]	# of DOFs
Full	44	$178 \cdot 10^3$
SLNS	6.8	$(110 + 55) \cdot 10^3$
Bossart	0.7	$2 \times 11 \cdot 10^3$
LRF	0.2	254

broadband absorption with tube resonators. This sample consists of 20 tubes (blind holes) with different radii and lengths. Only the dark gray boundaries in the figure are modeled as walls with viscothermal effects. The light gray boundaries (impedance tube and resonator ends) are modeled without viscothermal effects (slip, adiabatic) to reduce the required degrees of freedom: the mesh can be relatively coarse near these boundaries, since the boundary layer effects are not triggered.

The absorption coefficient curves of this sample are shown in Figure 11. Three models agree: the full model, the SLNS model and Bossart's model. These models also

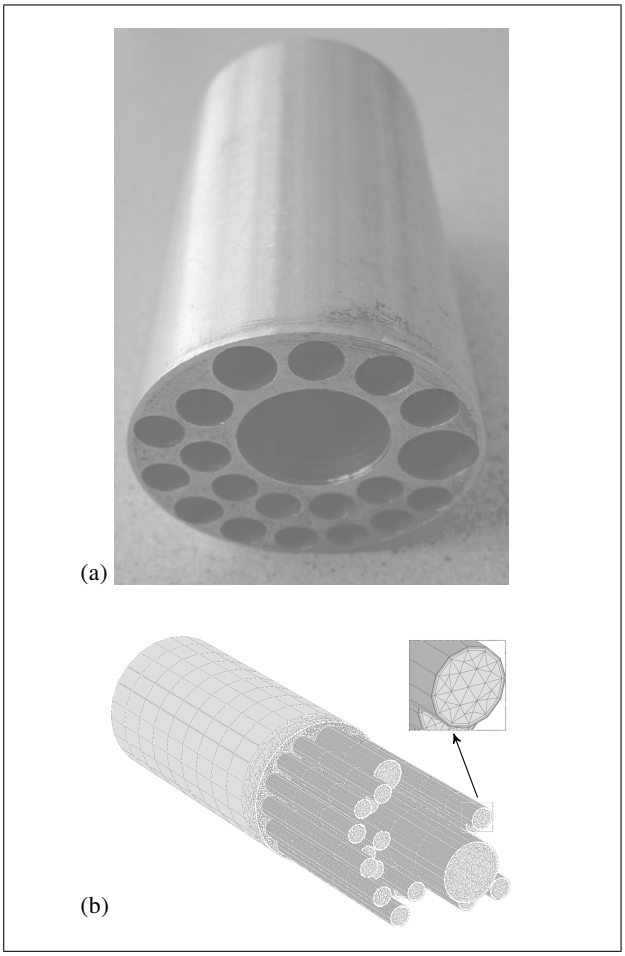

Figure 10. Hannink's sample. (a) Photo, (b) FEM model.

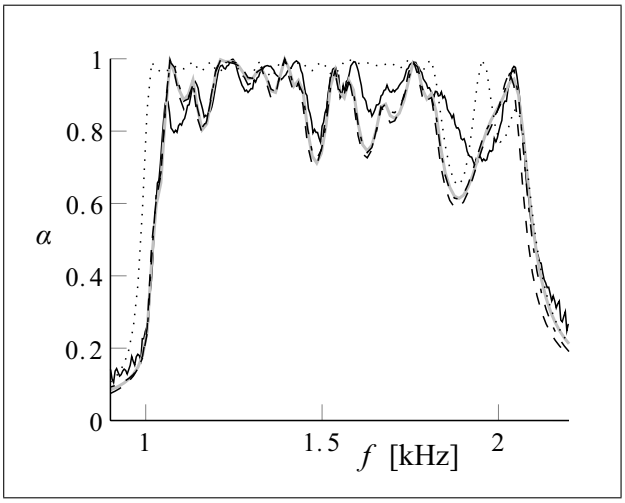

Figure 11. Absorption coefficient of Hannink's sample: (——) measurement; (——) full model; (– – –) SLNS model; (– - –) Bossart's model; (· · ·) LRF model.

agree to the measured curve, but not as well as for the previous sample. The curve of the low reduced frequency model is less accurate, because it does not account for the complicated 3-D effects of the acoustic field at the surface of the sample where all tubes meet.

Table IV. Calculation time per frequency and number of DOFs for the different models of Hannink's sample. The full and SLNS models use the same FEM mesh.

Model	t_c [s]	# of DOFs
Full	1926	$584 \cdot 10^3$
SLNS	148	$3 \times 141 \cdot 10^3$
Bossart	24	$2 \times 54 \cdot 10^3$
LRF	0.001	22

The computational costs are listed in Table IV. The SLNS model is now 13 times faster than the full model, with identical FEM meshes. This reduction is larger than for the previous sample, because this model is 3-D. Bossart's model is again faster than both the full and the SLNS models, because a coarser mesh can be used, and for this sample it is comparably accurate. The LRF is very fast because analytic solutions are used for each tube. Only 22 degrees of freedom are needed to couple the tubes. The LRF model is not as accurate as the other models, but it may be sufficient for certain purposes.

3.2. Moving walls

Two models with moving walls and fluid structure interaction are presented next. The first model represents a condenser microphone and the second model describes small drums. Both models use a membrane as the structure. Therefore the model of the membrane is introduced first.

3.2.1. Membrane model

The membrane in the models with moving walls is modeled at a boundary of the fluid domain. Therefore, the dimensionality of the membrane model is one lower than of the fluid: the membrane is 2-D if the fluid is 3-D and it is 1-D if the fluid is 2-D. The boundary of the fluid that contains the membrane is indicated by the symbol $\partial\Omega_m$. A membrane with a uniform tension can be described by the Helmholtz equation, see for example [9],

$$\sigma_m \Delta \dot{u} + \sigma_m k_m^2 \dot{u} = \mathrm{i}\omega \left(P_m - p\right), \tag{31}$$

with wave number

$$k_m^2 = \frac{\omega^2 \rho_m}{\sigma_m}. \tag{32}$$

The symbol $\dot{u}$ is the normal velocity field of the membrane [m/s], σ_m is the tension in the membrane in [N/m], ρ_m the mass per unit surface [kg/m^2]. Furthermore, P_m is the external load on one side of the membrane and p is the pressure of the fluid on the other side of the membrane, both in [Pa]. This pressure p is calculated with the fluid model. Additionally, the velocity of the membrane is prescribed as a boundary condition to the fluid:

$$\dot{u} = \boldsymbol{v} \cdot \boldsymbol{n} \quad \text{at } \partial\Omega_m \tag{33}$$

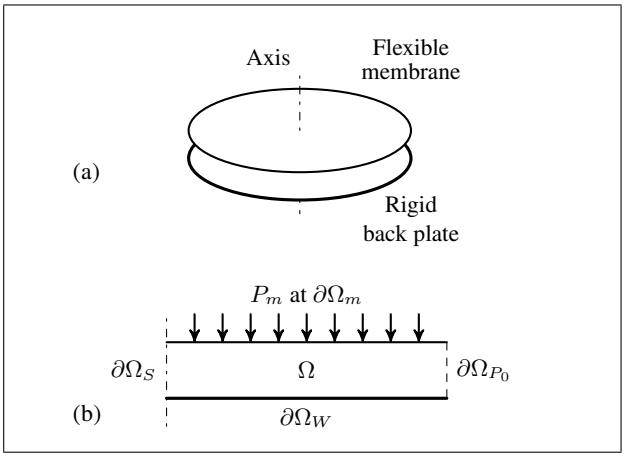

Figure 12. Condenser microphone (a) and axi-symmetric model (b). $\partial\Omega_m$ is the boundary with the membrane. The radius of the membrane is 2 mm, and the air layer thickness is 18 μm.

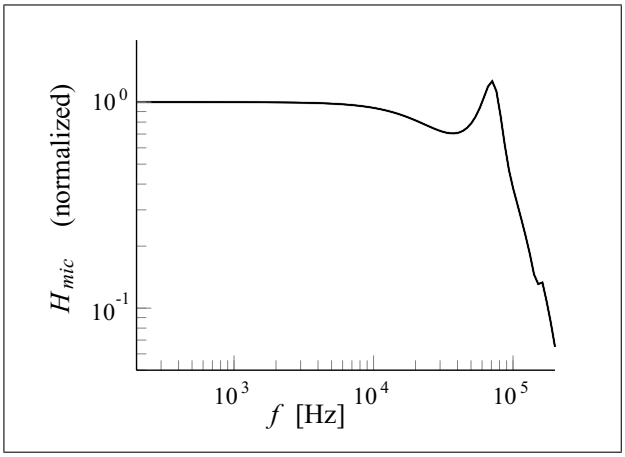

Figure 13. The normalized sensitivity of the microphone. The plot contains four nearly coincident lines: the analytic model of Plantier/Cutanda, the full model, the SLNS model and the LRF model.

3.2.2. Condenser microphone

Figure 12 shows the axi-symmetric model of a simple condenser microphone. It contains a thin layer of air between a rigid backplate and a flexible membrane. A harmonic uniform pressure on top of the membrane deflects the membrane and pushes air out of the layer. A zero pressure boundary conditions is used at the circumference of the air layer.

The results of four different models are compared. These are the full model, the new SLNS model, the low reduced frequency model and the analytic model of Plantier [18] with the source code that is listed in the in the appendix of the PhD thesis [14] of Cutanda Henríquez[1]. The normal velocity inconsistency in the SLNS model is untreated: neither of the two presented rules is used in this model. Figure 13 compares the calculated normalized sensitivities H_{mic}, which is defined as the normalized mean membrane displacement. The four curves in the figure overlap perfectly. Therefore, the inconsistency in the normal velocity of the SLNS model does not lead to large errors in this case. An explanation is that the problem is a squeeze film type in which the pressure gradient normal to the membrane is very small compared to the pressure gradient in the radial direction. Relatively large errors in the normal pressure gradient remain small compared to the radial pressure gradient.

3.2.3. Drums

The second model with moving walls resembles the first model, but has an air geometry that is more like a drum than like the thin layer of the microphone model. Figure 14 shows the geometry of the problem with two different sets of boundary conditions: the open drum and the closed drum. Several meshes are used and the finest and coarsest meshes are shown in Figure 15. Notice that the coarsest mesh is already quite fine.

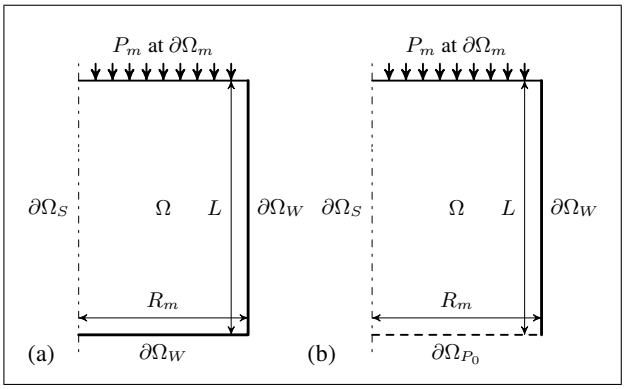

Figure 14. Axi-symmetric fluid structure interaction problems used to discuss the normal velocity inconsistency in the SLNS model, with $R_m = 2$ mm and $L = 3$ mm. (a) Closed drum, (b) Open drum.

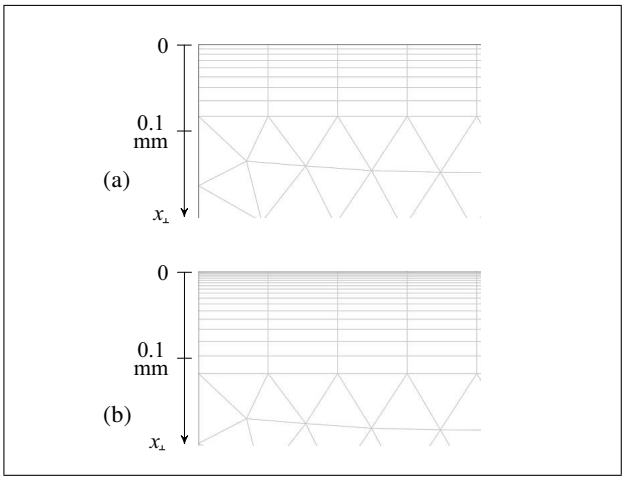

Figure 15. The coarsest and finest boundary layer mesh used for the SLNS model. Only a small area near the membrane center is shown. (a) Coarsest mesh, (b) Finest mesh.

[1] The PhD thesis of Cutanda Henríquez presents a viscothermal acoustic BEM model for arbitrary geometries that is based on the classical Kirchhoff solution method of viscothermal acoustics. Figure 25-5 of this thesis corresponds to Figure 13 of this paper. The SLNS model performs well in this indirect comparison.

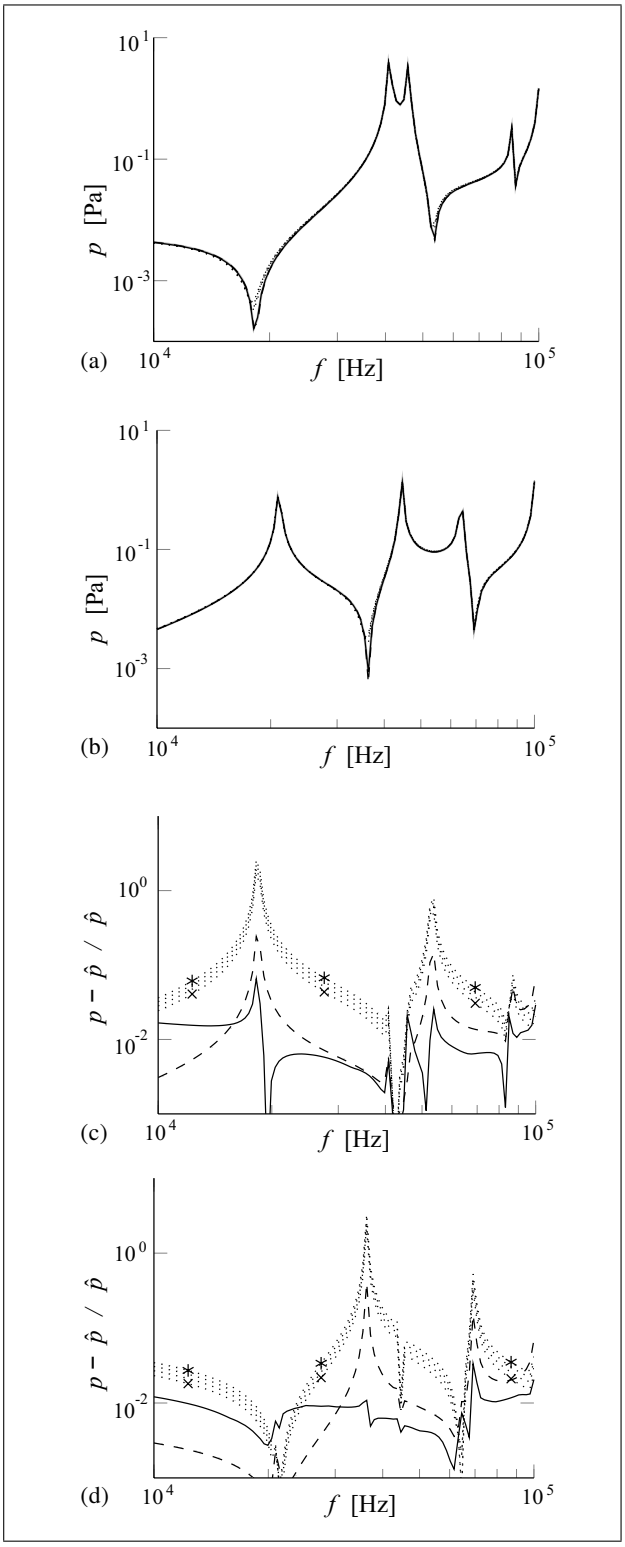

Figure 16. Pressure magnitude at the center of the membrane versus the frequency in (a) and (b); normalized difference with the full model as the reference solution $\hat{p}$ in (c) and (d); (——) full model; (——) Bossart's model; (4×···) SLNS models (finest mesh ∗ and coarsest mesh ×); (– – –) SLNS model with a slip BC at the membrane. (a) and (c) closed drum, (b) and (d) open drum.

The resulting magnitude of the pressure in the air at the center of the membrane is shown in Figure 16. The differences between the curves are just visible in the plot. Therefore, this figure also shows the relative error with the full model on the finest mesh as the reference solution. These plots show that the largest errors occur at the pressure anti-resonances. Furthermore, these plots show that the two countermeasures presented in section 2.3.4 prove to be beneficial: the errors reduce if slip boundary conditions are used or if coarser meshes are used. Still, the result without these countermeasures may be sufficiently accurate.

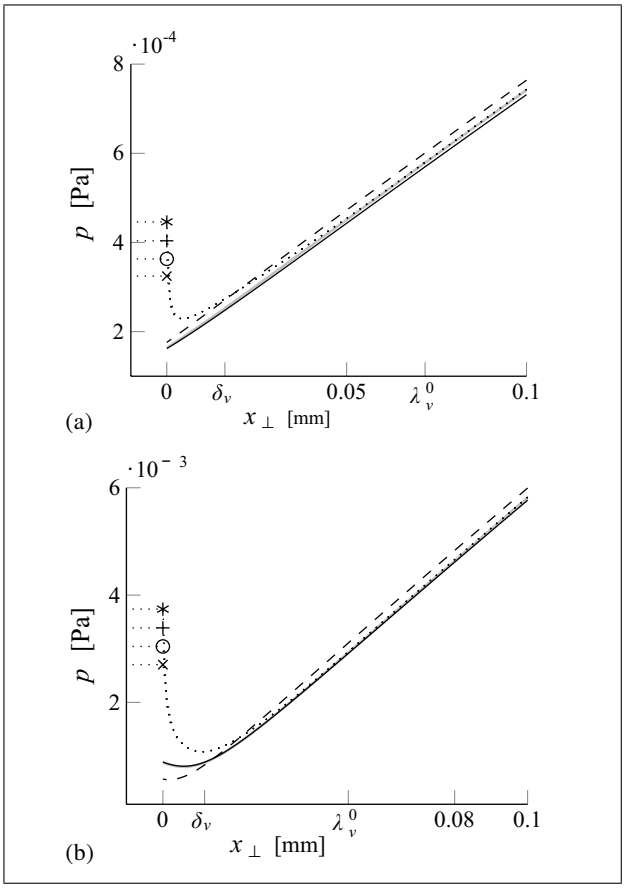

Figure 17. The pressure magnitude versus the coordinate $x_\perp$: The full model (——); Bossart's model (——); SLNS model with slip BC (– – –); untreated SLNS models (4×···) (× coarsest mesh and ∗ finest mesh). (a) Closed drum, 18.2 kHz, (b) Open drum, 36.3 kHz.

Additional insight in the error caused by the normal velocity inconsistency can be obtained by plotting the pressure magnitude along the axis of symmetry of the models at the worst case frequencies. These curves are shown in Figure 17. Only very close to the boundary do the SLNS models yield an erroneous pressure. Neglecting the viscous effects at the membrane reduces the error at the boundary, but introduces a small error in the domain.

The coarsest mesh of the drum problem is still rather fine. It has a layer that contains eight quadrilateral elements; see Figure 15. The pressure field does not need such a fine mesh; it is only needed for the viscous and thermal fields. Therefore, it is interesting to see if the accuracy of the SLNS model can be further improved by us-

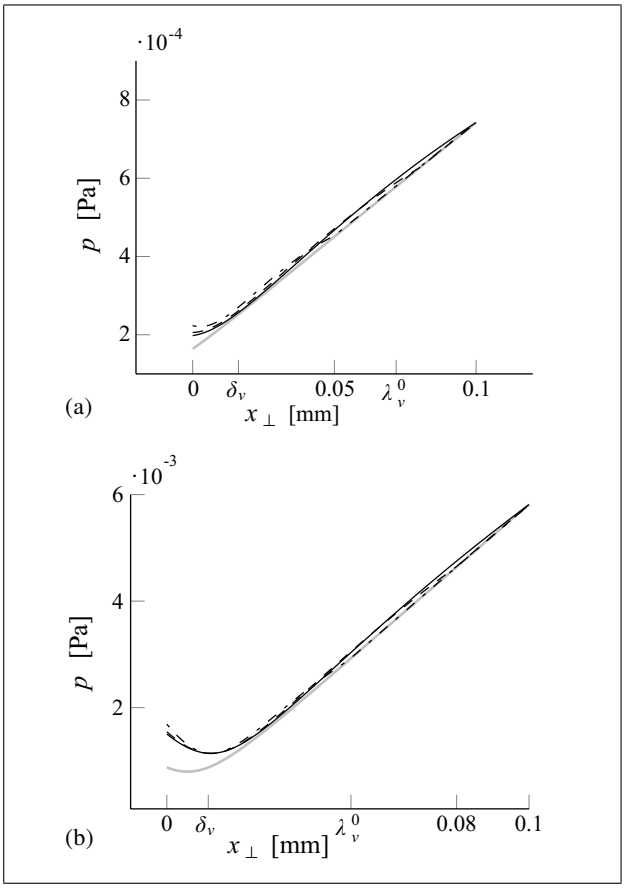

Figure 18. The pressure magnitude versus the coordinate $x_\perp$ for the SLNS model with a coarse pressure mesh and high order numerical integration: (——) full model; (——) coarse mesh SLNS model with 0.1 mm element thickness; (– – –) with 0.08 mm element thickness; (– - –) with 0.05 mm element thickness. (a) Closed drum, 18.2 kHz, (b) Open drum, 36.3 kHz.

ing a much coarser mesh for the pressure calculation with single layer of quadrilateral elements. The thickness of the elements in this layer is varied from 0.05 to 0.1 mm. Figure 18 plots the pressure magnitude along the axis for these element sizes. This figure shows that the error is spread out over the area of the first element. Moreover, the error at the membrane (at $x_\perp = 0$) is much lower than in Figure 17. To get these results, the order of the numerical integration is increased to accurately capture the contribution of the viscous and thermal fields in the pressure calculation. The viscous and thermal fields are defined in these calculations by the analytic expression

$$\Psi_\phi = 1 - \mathrm{e}^{-\mathrm{i}k_\phi x_\perp}, \tag{34}$$

with $x_\perp$ the distance to the nearest boundary.

4. Conclusions

A new approximate model for viscothermal acoustics has been presented, called the SLNS model. Although the new model is computationally less efficient than the LRF model and Bossart's model, it is more efficient than the fully coupled model of viscothermal acoustics. Because the new model is applicable to arbitrary geometries, unlike other approximate models that the authors are aware of, it is a useful addition to the range of viscothermal acoustic models.

A practical application for the SLNS model may the modeling of miniature acoustic transducers. These transducers may be too small to model with Bossart's model and too irregularly shaped to use the LRF model. Furthermore, it is relatively straightforward to couple the SLNS FEM model to mechanical FEM models of, for example, a membrane of such a transducer.

The SLNS model contains an inconsistency in the normal velocity at no-slip walls with non-zero normal velocity. This inconsistency does lead to errors, but these are small in the shown application. Furthermore, two countermeasures are presented that effectively reduce these errors still. The authors did not yet find a problem in which the errors are unacceptably high.

Appendix

A1. Order of magnitude analyses

The missing parts in the derivation of the SLNS model are presented in this appendix.

A1.1. Dimensionless equations

The order of magnitude analyses are conveniently done with dimensionless equations. The dimensionless fields and operators are defined as

$$\tilde\nabla \equiv k_0^{-1}\nabla, \quad \tilde\Delta \equiv k_0^{-2}\Delta, \tag{A1a}$$
$$\tilde k_v \equiv k_v/k_0, \quad \tilde k_h \equiv k_h/k_0, \tag{A1b}$$
$$\tilde p \equiv p/p_0, \quad \tilde{\boldsymbol v} \equiv \gamma \boldsymbol v/c_0, \tag{A1c}$$
$$\tilde T \equiv \frac{\gamma T/T_0}{\gamma - 1}, \quad \tilde\xi \equiv 1 + \lambda/\mu. \tag{A1d}$$

These dimensionless parameters are chosen such that $\tilde p$, $\tilde{\boldsymbol v}$ and $\tilde T$, and their gradients, for example $\left|\tilde\nabla\tilde T\right|$, are of equal magnitude for an isentropic acoustic plane wave solution. The governing equations (1) in the above dimensionless parameters read

$$\tilde{\boldsymbol v} + \tilde\xi\tilde k_v^{-2}\tilde\nabla(\tilde\nabla\cdot\tilde{\boldsymbol v}) + \tilde k_v^{-2}\tilde\Delta\tilde{\boldsymbol v} = \mathrm{i}\tilde\nabla\tilde p, \tag{A2a}$$
$$\tilde T + \tilde k_h^{-2}\tilde\Delta\tilde T = \tilde p, \tag{A2b}$$
$$-\mathrm{i}\tilde\nabla\cdot\tilde{\boldsymbol v} + \gamma\tilde p - (\gamma-1)\tilde T = 0. \tag{A2c}$$

Orders of magnitude are expressed with the wave numbers $\tilde k_\phi$ (with ϕ replaced by v or h), for example: if $\left|\tilde T\right|$ is the reference, then $\left|\tilde k_h\tilde T\right|$ is first order large and $\left|\tilde k_h^{-2}\tilde T\right|$ is second order small.

A1.2. Simplifying the momentum equation

Since $\tilde k_v \gg 1$ and $\tilde k_h \gg 1$, the only significant terms in the above set for the isentropic acoustic plane wave solution are those that do not contain divisions by these wave

numbers:

$$\tilde{\boldsymbol{v}} = \mathrm{i}\tilde{\nabla}\tilde{p}, \tag{A3a}$$

$$\tilde{T} = \tilde{p}, \tag{A3b}$$

$$-\mathrm{i}\tilde{\nabla}\cdot\tilde{\boldsymbol{v}} + \tilde{p} = 0, \tag{A3c}$$

where the temperature solution is substituted into the continuity equation to get the displayed result. The dimensionless isentropic acoustic Helmholtz equation results if the velocity solution is substituted into the continuity equation as well.

The above set of equations is valid for a plane wave. The approximations are not valid for evanescent waves and near point sources. In these cases, the velocity and their derivatives can be very large, and neglecting the corresponding terms in the momentum equation is incorrect. Nevertheless, the resulting Helmholtz equation is widely accepted as an accurate model of isentropic acoustics. Pierce [8] elaborates on these issues. In the derivation of the SLNS model, the assumption that such localized large gradients can be neglected is made as well, just like in isentropic acoustics.

The equations are more complicated for isentropic acoustics. Only the term containing $\tilde{\xi}$ is known to be small as mentioned in the main text. Near boundaries, the normal derivative of the temperature and (shear) velocity (*not* of the pressure) can be much larger than the field itself; about a factor $\left|k_h\right|$ or $\left|k_v\right|$ larger. Simply put: each spatial derivation may increase the result an order of magnitude. An exception is the divergence of the velocity that is of the same order of magnitude as the pressure and temperature, as the continuity equation states. Therefore, the term that contains $\tilde{\xi}$ is first order small and can be neglected ($\tilde{\xi}$ itself is approximately unity). This yields the following set of governing equations:

$$\tilde{\boldsymbol{v}} + \tilde{k}_v^{-2}\tilde{\Delta}\tilde{\boldsymbol{v}} = \mathrm{i}\tilde{\nabla}\tilde{p}, \tag{A4a}$$

$$\tilde{T} + \tilde{k}_h^{-2}\tilde{\Delta}\tilde{T} = \tilde{p}, \tag{A4b}$$

$$-\mathrm{i}\tilde{\nabla}\cdot\tilde{\boldsymbol{v}} + \gamma\tilde{p} - (\gamma-1)\tilde{T} = 0. \tag{A4c}$$

This set is the dimensionless form of the set (6). Neglecting the term that contains $\tilde{\xi}$ also leads to the reduced expression (5) of the divergence of the viscous tensor.

A1.3. Approximate solutions

Next, the approximate solutions (9) and (10) should be validated. In dimensionless form, these solutions are

$$\tilde{\boldsymbol{v}}_{\parallel} = \mathrm{i}\Psi_v\tilde{\nabla}_{\parallel}\tilde{p}, \tag{A5a}$$

$$\tilde{T} = \Psi_h\tilde{p}. \tag{A5b}$$

The viscous and thermal fields were already dimensionless. Like with the temperature and the shear velocity, the spatial derivatives of the viscous and thermal fields are expected to be an order larger than these fields themselves. Substitution of the above temperature solution into the entropy equation yields

$$\left(\Psi_h + \tilde{k}_h^{-2}\tilde{\Delta}\Psi_h\right)\tilde{p} + \tilde{k}_h^{-2}\left(2\tilde{\nabla}\Psi_h\cdot\tilde{\nabla}\tilde{p} + \Psi_h\tilde{\Delta}\tilde{p}\right) = \tilde{p}. \tag{A6}$$

The second term at the left-hand side is first order small and can be neglected. This leaves

$$\left(\Psi_h + \tilde{k}_h^{-2}\tilde{\Delta}\Psi_h\right)\tilde{p} = \tilde{p}. \tag{A7}$$

Therefore, the approximate solution of the temperature is accurate if the thermal field satisfies (12). The validation of the shear velocity solution is similar and not presented.

A1.4. Approximate boundary conditions

The last thing to show is that the approximate adiabatic and no-shear-force boundary conditions are accurate. The exact adiabatic boundary condition results from substitution of the approximate solution into $\tilde{\nabla}_n\tilde{T} = 0$, and reads

$$\tilde{\nabla}_n\Psi_h = -\Psi_h\frac{\tilde{\nabla}_n\tilde{p}}{\tilde{p}}. \tag{A8}$$

The approximation of the right hand side as zero is accurate because $\left|\tilde{\nabla}_n\tilde{p}/\tilde{p}\right| \ll \left|\tilde{k}_h\right|$ where $\left|\tilde{k}_h\right|$ is the magnitude that is expected for $\tilde{\nabla}_n\Psi_h$ near an isothermal wall. Furthermore, the small error in the above approximation only influences a small region near the boundary and does not affect the solution further than a boundary layer thickness away. The approximate slip boundary condition results from a similar derivation.

Acknowledgement

The support of *Sonion* is gratefully acknowledged.

References

[1] W. R. Kampinga, Y. H. Wijnant, A. de Boer: Performance of several viscothermal acoustic finite elements. Acta Acustica united with Acustica **96** (2010) 115–124(10).

[2] M. Malinen, M. Lyly, P. Råback, A. Kärkkäinen, L. Kärkkäinen: A finite element method for the modeling of thermo-viscous effects in acoustics. Proceedings of ECCOMAS, Jyväskylä, Finland, 2004.

[3] N. Joly: Finite element modeling of thermoviscous acoustics on adapted anisotropic meshes: Implementation of the particle velocity and temperature variation formulation. Acta Acustica united with Acustica **96** (2010) 102–114(13).

[4] W. M. Beltman: Viscothermal wave propagation including acousto-elastic interaction. Dissertation. University of Twente, Enschede, The Netherlands, 1998.

[5] W. M. Beltman: Viscothermal wave propagation including acousto-elastic interaction, part I: theory. Journal of Sound and Vibration **227** (1999) 555–586.

[6] H. Tijdeman: On the propagation of sound waves in cylindrical tubes. Journal of Sound and Vibration **39** (1975) 1–33.

[7] R. Bossart, N. Joly, M. Bruneau: Hybrid numerical and analytical solutions for acoustic boundary problems in thermo-viscous fluids. Journal of Sound and Vibration **263** (2003) 69–84.

[8] A. D. Pierce: Acoustics: An introduction to its physical principles and applications. Acoustical Society of America, 1991.

[9] P. M. Morse, K. U. Ingard: Theoretical acoustics. McGraw-Hill, 1968.

[10] M. Bruneau, P. Herzog, J. Kergomard, J. D. Polack: General formulation of the dispersion equation in bounded visco-thermal fluid, and application to some simple geometries. Wave Motion **11** (1989) 441–451.

[11] H. Inayat Hussain: Thermoviscous effects in acoustic radiation problems. Dissertation. l'Institut National des Sciences Appliquées de Lyon, Lyon, France, 2009.

[12] F. P. Mechel: Revision of the Kirchhoff-Rayleigh-theory of sound propagation in visco-thermal air. part I: Basic equations and capillary modes. Acta Acustica united with Acustica **93** (2007) 507–534.

[13] L. Cremer: Über die akustische Grenzschicht vor starren Wänden. Archiv der elektrischen Übertragung **2** (1948) 136–139.

[14] V. Cutanda Henríquez: Numerical transducer modeling. Dissertation. Technical University of Denmark (DTU), Lyngby, Denmark, 2002.

[15] Comsol Multiphysics user's guide. 3.5 ed. 2008.

[16] J. F. J. Jansen: Viscous and thermal behavior of acoustic wave propagation. Diploma Thesis. University of Twente, Enschede, The Netherlands, 2009.

[17] M. H. C. Hannink, Y. H. Wijnant, A. de Boer: Optimized sound absorbing trim panels for the reduction of aircraft cabin noise. Proceedings of ICSV 11, St. Petersburg, Russia, 2004.

[18] G. Plantier, M. Bruneau: Heat conduction effects on the acoustic response of a membrane separated by a very thin air film from a backing electrode. Journal d'acoustique **3** (1990) 243–250.